ACS APPLIED MATERIALS & INTERFACES

Research Article

www.acsami.org

Enhanced Performance of Perovskite $CH_3NH_3PbI_3$ Solar Cell by Using CH_3NH_3I as Additive in Sequential Deposition

Yian Xie,[†,‡] Feng Shao,[†,§] Yaoming Wang,[†] Tao Xu,*[,∥] Deliang Wang,[§] and Fuqiang Huang*[,†,‡]

[†]CAS Key Laboratory of Materials for Energy Conversion, Shanghai Institute of Ceramics, Chinese Academy of Sciences, Shanghai 200050, People's Republic of China

[‡]State Key Laboratory of Rare Earth Materials Chemistry and Applications, College of Chemistry and Molecular Engineering, Peking University, Beijing 100871, People's Republic of China

[§]Hefei National Laboratory for Physical Sciences at the Microscale, University of Science and Technology of China, Hefei 230026, People's Republic of China

[∥]Department of Chemistry and Biochemistry, Northern Illinois University, DeKalb, Illinois 60115, United States

Supporting Information

ABSTRACT: Sequential deposition is a widely adopted method to prepare $CH_3NH_3PbI_3$ on mesostructured TiO_2 electrode for organic lead halide perovskite solar cells. However, this method often suffers from the uncontrollable crystal size, surface morphology, and residual PbI_2 in the resulting $CH_3NH_3PbI_3$, which are all detrimental to the device performance. We herein present an optimized sequential solution deposition method by introducing different amount of CH_3NH_3I in PbI_2 precursor solution in the first step to prepare $CH_3NH_3PbI_3$ absorber on mesoporous TiO_2 substrates. The addition of CH_3NH_3I in PbI_2 precursor solution can affect the crystallization and composition of PbI_2 raw films, resulting in the variation of UV−vis absorption and surface morphology. Proper addition of CH_3NH_3I not only enhances the absorption but also improves the efficiency of $CH_3NH_3PbI_3$ solar cells from 11.13% to 13.37%. Photoluminescence spectra suggest that the improvement of device performance is attributed to the decrease of recombination rate of carriers in $CH_3NH_3PbI_3$ absorber. This current method provides a highly repeatable route for enhancing the efficiency of $CH_3NH_3PbI_3$ solar cell in the sequential solution deposition method.

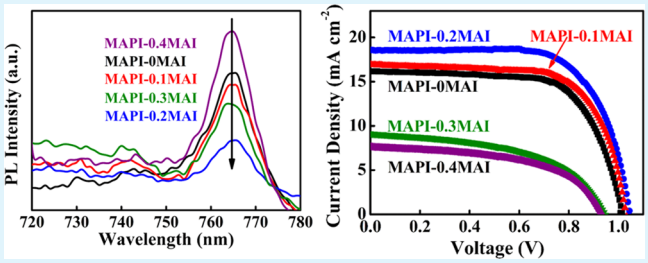

KEYWORDS: *perovskite, solar cell, sequential solution deposition, recombination, CH_3NH_3I*

INTRODUCTION

In the last 5 years, organic−inorganic hybrid perovskites (e.g., $CH_3NH_3PbI_3$) have gained extensive attention around the world, and high power conversion efficiency close to 20%[1,2] is achieved by these perovskites-based solar cells, which is comparable to commercialized c-Si solar cells and state of the art $Cu(In,Ga)(S,Se)_2$ thin film photovoltaic solar cells.[3] $CH_3NH_3PbI_3$ perovskite affords several important advantages such as high absorption coefficient ($>10^4$ cm^{-1}),[4,5] highly mobile electron and holes,[6] long carrier transport diffusion length (100−1000 nm),[5,7,8] and suitable and tunable direct band gap by controlling the chemical composition,[9−11] making it an outstanding light harvester and an excellent hole transport material. Furthermore, $CH_3NH_3PbI_3$ solar cells can be fabricated via simple and low-cost chemical solution methods, which has great potential in large-scale production.

Presently, the most adapted and traditional chemical solution deposition methods can be classified into two categories, namely, one-step deposition and sequential deposition methods. As for a one-step deposition method, Cl is a powerful additive in precursor solution with the forms including $PbCl_2$[12,13] or CH_3NH_3Cl.[14] The addition of Cl can slow down the crystallization rate during the annealing process and thus control the morphology of $CH_3NH_3PbI_{3-x}Cl_x$ thin films. Although high-efficiency $CH_3NH_3PbI_{3-x}Cl_x$ solar cells have been successfully constructed by a one-step deposition method, the atomic ratio of Cl in the perovskite as well as the reaction mechanism that leads to its formation and crystallization are still under debate.[15−17] In a typical sequential deposition process, PbI_2 layer or film is first deposited on a compact TiO_2 layer or mesoporous TiO_2 layer from its *N*,*N*-dimethylformamide (DMF) solution, followed by immersing the PbI_2 film in a CH_3NH_3I (MAI) 2-propanol solution to form the desired $CH_3NH_3PbI_3$. However, two main problems are found in sequential deposition. First, the crystal size and surface morphology of $CH_3NH_3PbI_3$ are uncontrollable, which is detrimental to device reproducibility. Second, the residual PbI_2 in $CH_3NH_3PbI_3$ thin films deteriorates the reproducibility of

Received: March 28, 2015
Accepted: May 26, 2015
Published: May 26, 2015

DOI: 10.1021/acsami.5b02705
ACS Appl. Mater. Interfaces 2015, 7, 12937−12942

device performance as well. Although some work tackled this problem, including depositing a high-coverage $CH_3NH_3PbI_3$ capping layer on mesoporous TiO_2 films by spin coating the PbI_2 layer twice[18] or using dimethyl sulfoxide (DMSO) as the solvent for better film quality,[19] a more reliable access to acquire $CH_3NH_3PbI_3$ with less structural defects is still exceptionally desired.

In this work, we developed an alternative approach to tackle this problem. We introduced a certain amount of MAI in the precursory PbI_2 solution during the first step. The crystallization and surface morphology of $CH_3NH_3PbI_3$ became very sensitive to the addition of MAI, while a suitable amount of MAI can improve the absorption without disturbing the high coverage of the capping layer. In comparison to the devices without the addition of MAI in the first step, power conversion efficiency is enhanced from 11% to 13% under optimum addition amount of the initial MAI. The improvement in device performance can be due to the increase of short-circuit current (J_{sc}) and slight increase of open-circuit voltage (V_{oc}). The recombination rate of carriers is investigated by photoluminescence (PL) spectra.

EXPERIMENTAL DETAILS

Transparent Conducting Substrate and Mesoporous TiO_2 Thin Film. Fluorine-doped SnO_2-coated transparent conducting glass substrate (FTO) was washed by ultrasonication with detergent first, then washed with deionized water, acetone, and ethanol, and finally dried with dry nitrogen air. A 50 nm thick TiO_2 compact layer was then deposited on the substrates by sputtering at 0.6 Pa with 120 W for 30 min. The mesoporous TiO_2 film was prepared by spin coating a 20 nm sized TiO_2–nanoparticulate paste (diluted in ethanol with a ratio of 1:5 by weight, OPV-Tech, DHS-TPP3) 4 times at 2500 rpm for 30 s, dried at 125 °C for 10 min, then heated at 500 °C for 30 min.

Device Fabrication. CH_3NH_3I (MAI) was synthesized by reacting 19.5 mL of methylamine (40 wt % aqueous solution) and 32.3 mL of hydroiodic acid (55–58 wt % aqueous solution) in an ice bath for 2 h with stirring. The product was obtained by rotary evaporation at 45 °C and cleaning with diethyl ether followed by drying in a vacuum oven at 60 °C overnight.[20] Five precursory solutions were prepared by dissolution of 1 mmol of PbI_2 and 0, 0.1, 0.2, 0.3, or 0.4 mmol of MAI in 1 mL of DMF at 60 °C, which is labeled as PbI_2–xMAI (x = 0, 0.1, 0.2, 0.3, or 0.4, respectively). The precursors were spin coated on the mesoporous TiO_2 films at 6000 rpm for 10 s and then heated on a hot plate at 100 °C for 10 min. Subsequently, the films were infiltrated in 2-propanol and blow dried. Perovskite films were formed by immersing these PbI_2–xMAI films in a 10 mg/mL MAI 2-propanol solution for 25 min; the obtained perovskite films are labeled as MAPI–xMAI accordingly. After being rinsed with 2-propanol, the perovskite films were annealed at 100 °C for 10 min. The hole transport material (HTM) solution was prepared as followed: 52.8 mg of 2,29,7,79-tetrakis(*N*,*N*-di-*p*-methoxyphenylamine)-9,99-spirobifluorene (spiro-MeOTAD) was dissolved in 640 μL of chlorobenzene and mixed with 10 μL of 500 mg/mL bis(trifluoromethane)-sulfonimide lithium salt (LiTFSI) solution in acetonitrile and 14.4 μL of 4-*tert*-butylpyridine (TBP). The HTM solution was spin coated on the perovskite-covered TiO_2 electrodes at 2500 rpm for 30 s. For the counter electrode, 100 nm thick Au was deposited on top of the HTM layer by thermal evaporation and the active area was 0.07 cm^2.

Characterization. Crystallization and phase identification of the thin films were performed by X-ray diffraction (XRD Bruker D8 Focus) with a monochromatized source of Cu Kα1 radiation (λ = 0.15405 nm) at 1.6 kW (40 kV, 40 mA). UV–vis absorbance spectra were recorded on a Hitachi U-3010 spectrophotometer with a scanning velocity of 300 nm min^{-1}. Raman spectra were collected on a thermal dispersive spectrometer using a laser with an excitation wavelength of 532 nm at a laser power of 10 mW. Top-view field emission scanning electron microscopy (FESEM) images were taken on a ZEISS SUPRA 55 microscope. PL spectra were measured at 300 K on a fluorescence spectrophotometer (F-4600, Hitachi, Japan) with an excitation wavelength of 466 nm. Photocurrent density–voltage characteristics were measured using a Keithley model 2440 source meter under AM 1.5 illumination. A 1000 W Oriel solar simulator was used as a light source, and the power of the light was calibrated to 1 sun light intensity by using a NREL-calibrated Si cell (Oriel 91150). The scan rate was 57.5 mV s^{-1}, and the scan direction was from high to low voltage. The external quantum efficiency (EQE) was measured by a Newport QE system equipped with a 300 mW xenon light and a lock-in amplifier.

RESULTS AND DISCUSSION

XRD analysis was conducted to verify the crystallization of the PbI_2–xMAI and final $CH_3NH_3PbI_3$ layer on mesoporous TiO_2 films. The XRD patterns of PbI_2–xMAI films are shown in Figure 1a, and the detailed information between 11.5° and 15°

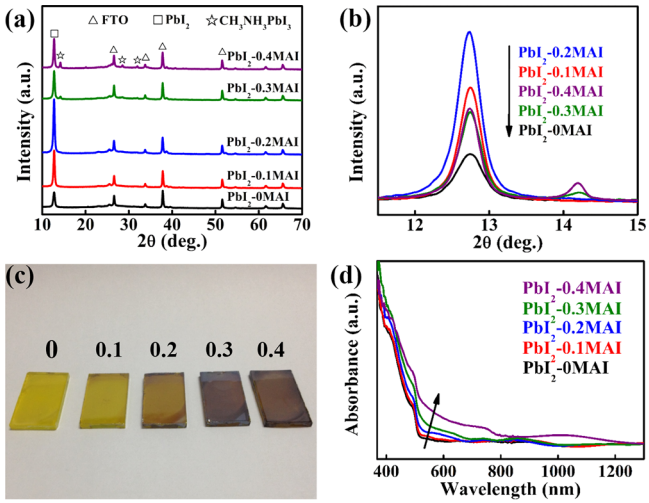

Figure 1. (a) XRD patterns and (b) detailed XRD information from 11° to 15° 2θ value of PbI_2–xMAI on mesoporous TiO_2 films with varying the x value (x = 0–0.4). The main XRD peaks of FTO, PbI_2, and $CH_3NH_3PbI_3$ were labeled. (c) Image and (d) UV–vis absorbance spectra of PbI_2–xMAI thin films as a function of x value.

is displayed in Figure 1b. As for PbI_2–0.1MAI and PbI_2–0.2MAI, the main peak of $CH_3NH_3PbI_3$ at 14.2° cannot be detected though a small amount of MAI was added in PbI_2 precursor solution (Figure 1b), which may result from the low crystallization of few $CH_3NH_3PbI_3$ and the decomposition of $CH_3NH_3PbI_3$ at high temperature (100 °C). On the other hand, the addition of small amount of MAI even led to better crystallization of PbI_2, indicated by the increasing peak intensity of PbI_2 at 12.7° in the range from PbI_2–0MAI to PbI_2–0.2MAI. The characteristic peak of $CH_3NH_3PbI_3$ at 14.2° was observed in PbI_2–0.3MAI, and this peak intensity increased in PbI_2–0.4MAI. The peak intensity of PbI_2 in these two samples decreased significantly compared with PbI_2–0.2MAI, which should be owing to the conversion of PbI_2 to $CH_3NH_3PbI_3$. Besides, the peak intensity of $CH_3NH_3PbI_3$ was much lower than that of PbI_2 even in PbI_2–0.4MAI, implying the low content of $CH_3NH_3PbI_3$ in the films. The color change can be observed (Figure 1c), and the absorption was measured by UV–vis spectra (Figure 1d). Not only did PbI_2's characteristic absorbance between 400 and 520 nm increase but also the absorbance between 520 and 780 nm from $CH_3NH_3PbI_3$ was enhanced gradually with increasing MAI. The enhancement of

DOI: 10.1021/acsami.5b02705
ACS Appl. Mater. Interfaces 2015, 7, 12937–12942

absorbance between 520 and 780 nm should be caused by the insertion of MAI in PbI_2 and the formation of $CH_3NH_3PbI_3$. Although there was no signal of $CH_3NH_3PbI_3$ detected in XRD patterns of PbI_2−0.1MAI and PbI_2−0.2MAI, MAI should be retained in thin films.

The corresponding $CH_3NH_3PbI_3$ films, denoted as MAPI−*x*MAI films, were formed by immersing these PbI_2−*x*MAI samples in a solution of 10 mg/mL MAI in 2-propanol, and their XRD patterns are collected in Figure 2a. There is a weak

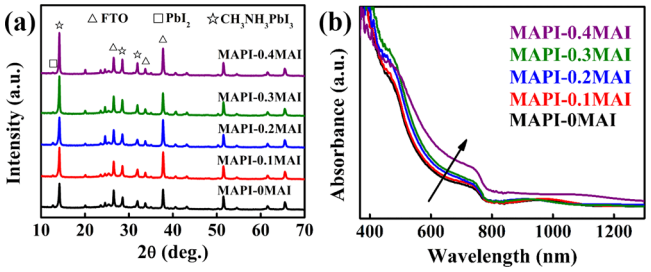

Figure 2. (a) XRD patterns and (b) UV−vis absorbance spectra of MAPI−*x*MAI thin films as a function of *x* value (*x* = 0−0.4).

signal of PbI_2 observed in the XRD of MAPI−0MAI, indicating incomplete conversion of PbI_2 to $CH_3NH_3PbI_3$, a common problem in sequential deposition.[19,21] However, residual PbI_2 was also found in other samples, suggesting that the conversion of PbI_2 to $CH_3NH_3PbI_3$ was not readily achieved, while a low content of $CH_3NH_3PbI_3$ was formed in PbI_2−*x*MAI (*x* = 0.3 or 0.4) beforehand. Derived from this, the low reaction driving force could be the main reason leading to the residue of PbI_2. Long dipping time was necessary to completely convert PbI_2 to $CH_3NH_3PbI_3$.[18] UV−vis spectra (Figure 2b) showed that the absorbance possessed a rinsing tendency in the visible light region (between 400 and 780 nm) from MAPI−0MAI to MAPI−0.3MAI. For MAPI−0.4MAI, it is noteworthy that the absorbance in the near-infrared region (>800 nm) was much higher than the previous four samples, which might result from surface scattering and lattice defects in $CH_3NH_3PbI_3$. Moreover, the absorbance between 400 and 500 nm was lower than that of MAPI−0.2MAI and MAPI−0.3MAI, manifesting the deteriorative absorption property occurring in MAPI−0.4MAI.

The further information on PbI_2−*x*MAI films was investigated by Raman spectroscopy, and the Raman spectra are shown in Figure S1a (see Supporting Information). For PbI_2−0MAI, the peak at 149 cm^{-1} was indexed to TiO_2 and the Raman peaks of PbI_2 were located at 76, 100, 114, and 172 cm^{-1}. With increasing CH_3NH_3I content in PbI_2 precursor, the peak intensity of PbI_2 at 172 cm^{-1} decreased and one small peak around 86−88 cm^{-1} appeared from PbI_2−0.2MAI to PbI_2−0.4MAI. Figure S1b, Supporting Information, shows the Raman spectra of MAPI−0.2MAI and mesoporous TiO_2 film. Comparing these two Raman spectra, the Raman signal from 70 to 130 cm^{-1} should be assigned to $CH_3NH_3PbI_3$. One small peak at 87 cm^{-1} was observed in MAPI−0.2MAI, and the position of this peak was consistent with the peak in Figure S1a, Supporting Information. Thus, the peak around 86−88 cm^{-1} in Figure S1a, Supporting Information, should be the signal of $CH_3NH_3PbI_3$. As for PbI_2−0.2MAI, although on signal of $CH_3NH_3PbI_3$ was found in XRD, the signal of $CH_3NH_3PbI_3$ was detected in Raman spectra.

The surface morphology and roughness of the PbI_2−*x*MAI films were measured by FESEM and AFM. The top-view FESEM images are shown in Figure S2, Supporting Information. For PbI_2−0MAI, the grain size was very small and almost no change in grain size was observed when $x \leq 0.2$. When $x \geq 0.3$, small dendritic grains were formed on the top of mesoporous TiO_2, the grain size increased with increasing *x* value, and even some mesoporous TiO_2 was exposed in PbI_2−0.4MAI. As shown in Figure S3, Supporting Information, the root-mean-square (RMS) values of surface roughness were 14.02, 8.15, 8.67, 59.31, and 74.29 nm for PbI_2−*x*MAI (*x* = 0, 0.1, 0.2, 0.3 and 0.4) films, respectively. PbI_2−0.1MAI and PbI_2−0.2MAI films were relatively smoother than regular PbI_2 film, while the surface roughness of PbI_2−0.3MAI and PbI_2−0.4MAI increased drastically. The increasing roughness of PbI_2−0.3MAI and PbI_2−0.4MAI were caused by the formation and crystal growth of $CH_3NH_3PbI_3$ phase on the surface. The surface morphology and roughness of the initial PbI_2−*x*MAI had a significant influence on the surface morphology of the subsequent MAPI−*x*MAI. The top-view morphologies of $CH_3NH_3PbI_3$ films prepared from different PbI_2−*x*MAI precursors were characterized by FESEM, and their images are shown in Figure 3a−e. The compact and hole-free capping

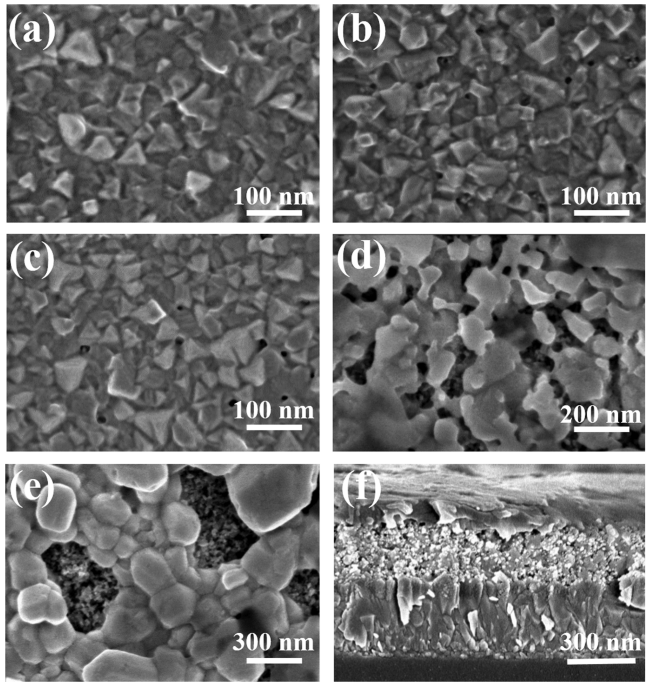

Figure 3. Top-view FESEM images of (a) MAPI−0MAI, (b) MAPI−0.1MAI, (c) MAPI−0.2MAI, (d) MAPI−0.3MAI, and (e) MAPI−0.4MAI and cross-sectional FESEM image of (f) MAPI−0.2MAI.

layers were achieved on MAPI−0MAI, MAPI−0.1MAI, and MAPI−0.2MAI films through sequential deposition. The morphologies of $CH_3NH_3PbI_3$ films based on MAPI−0MAI, MAPI−0.1MAI, and MAPI−0.2MAI films were quite similar to each other, and their crystal sizes were around 100 nm. In contrast, the MAPI−0.3MAI and MAPI−0.4MAI samples fabricated from these high RMS PbI_2−*x*MAI films had lots of pinholes and voids, and the grain size of the films increased to 150−200 and 200−300 nm, respectively. Thus, to achieve high surface coverage, the amount of MAI used in the first step should be kept in the relatively low region. The cross-sectional morphology of MAPI−0.2MAI is shown in Figure 3f. The

DOI: 10.1021/acsami.5b02705
ACS Appl. Mater. Interfaces 2015, 7, 12937−12942

thickness of the TiO_2 scaffold layer and $CH_3NH_3PbI_3$ capping layer was about 220 and 100 nm, respectively.

The PL spectra were effective in exploring the recombination properties of light-excited electrons and holes in semiconductors. Figure 4 shows the PL spectra of various MAPI−

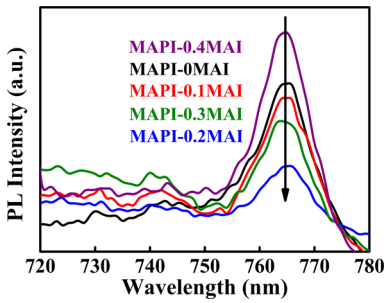

Figure 4. Steady-state PL spectra for MAPI−*x*MAI thin films with varying *x* value (*x* = 0−0.4).

*x*MAI samples. All samples' emission peaks were located at 764 nm (excitation wavelength 446 nm), consistent with previous reports of emission from $CH_3NH_3PbI_3$,[18,22,23] and the peak position of the emission was consistent among all of the samples. However, their PL intensities varied a lot and exhibited a decreasing tendency from MAPI−0MAI to MAPI−0.2MAI and an increasing tendency from MAPI−0.2MAI to MAPI−0.4MAI. The MAPI−0.2MAI showed the lowest peak intensity, a strong indication for low recombination and thus prospectively better photovoltaic performance.[24] In contrast, MAPI−0.4MAI exhibited the highest PL signal and thus a higher recombination rate of carriers in comparison to other samples.

In current−voltage (*J*−*V*) curve measurement, the curve shape can be affected by scan rate significantly, as shown in Figure S4 and Table S1, Supporting Information. In order to obtain a conventional *J*−*V* curve and avoid long time radiation, a scan rate of 57.5 mV s^{-1} was applied in the *J*−*V* curve measurement. Figure 5a shows the typical *J*−*V* curves of the

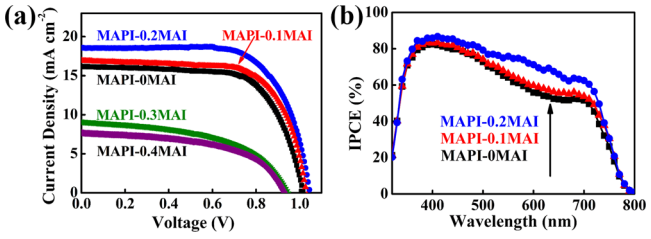

Figure 5. (a) Current−voltage (*J*−*V*) curves of the MAPI−*x*MAI-based (*x* = 0−0.4) solar cells under a standard AM 1.5 solar illumination at an intensity of 100 mW cm^{-2}. (b) IPCE spectra of the MAPI−*x*MAI-based (*x* = 0−0.2) solar cell without any applied bias.

MAPI−*x*MAI-based devices, and the device performance parameters are summarized in Table 1. The MAPI−0MAI-based cell exhibited a short-circuit photocurrent density (J_{sc}) of 16.15 mA cm^{-2}, open-circuit voltage (V_{oc}) of 1.015 V, and fill factor (FF) of 67.9%, yielding a power conversion efficiency of 11.13%. The efficiency increased to 11.92% and 13.37% for the MAPI−0.1MAI and MAPI−0.2MAI cells, respectively. Considering the similar FF values, the efficiency enhancement was mainly contributed by the higher J_{sc} and V_{oc}. The J_{sc} for MAPI−0.1MAI and MAPI−0.2MAI increased to 16.90 and 18.58 mA

Table 1. Summary of MAPI−*x*MAI-Based Solar Cell Performance Parameters with Varying *x* Values

sample	V_{oc} (V)	J_{sc} (mA cm^{-2})	*FF* (%)	η (%)
MAPI−0MAI	1.015	16.15	67.9	11.13
MAPI−0.1MAI	1.030	16.90	68.5	11.92
MAPI−0.2MAI	1.046	18.58	68.8	13.37
MAPI−0.3MAI	0.943	9.11	50.8	4.38
MAPI−0.4MAI	0.929	7.67	53.7	3.83

cm^{-2}, respectively, which was due to their stronger light absorption than MAPI−0MAI cell as shown in Figure 2b. The slight increase of V_{oc} from 1.030 V in the MAPI−0.1MAI cell to 1.046 V in the MAPI−0.2MAI cell should be owing to the less radiative recombination in the absorber of the MAPI−0MAI cell as manifested in Figure 4.[1,25] On the other hand, excessive addition of MAI (*x* = 0.3 and 0.4) in the first step had an adverse impact on device performance, as evidence by the sharp drop of J_{sc} and *FF* for MAPI−0.3MAI and MAPI−0.4MAI due to the high R_{RMS} and low coverage of $CH_3NH_3PbI_3$ capping layer, leading to more defective trap states for charge transport. According to the surface morphology, the lower device performance of MAPI−0.3MAI and MAPI−0.4MAI was due to the shunt leak through the pinholes in the $CH_3NH_3PbI_3$, through which the subsequent hole-transport materials can be in direct contact with the TiO_2. The averaged photovoltaic parameters extracted from *J*−*V* curves are collected in Figure S5, Supporting Information; V_{oc}, J_{sc}, *FF*, and efficiency exhibited a similar tendency on *x* value in the MAPI−*x*MAI. The low error bars indicated the good repeatability of our device fabrication procedures, in favor of the high confidence level of this study. In addition, hysteresis is observed in the MAPI−0.2MAI-based solar cell, as shown in Figure S6 and Table S2, Supporting Information.

The incident-photon-to-current conversion efficiency (IPCE) spectra (Figure 5b) revealed that the efficiency of MAPI−0MAI was higher than 80% in the range of 370−440 nm and dropped to lower than 60% in the range of 580−720 nm. The onset of photocurrent at 800 nm was consistent with the optical band gap of $CH_3NH_3PbI_3$.[26] The lower IPCE efficiency at long wavelength arose from inefficient charge extraction and/or light harvesting,[27] resulting in the relatively lower J_{sc} of solar cells. The MAPI−*x*MAIs with *x* = 0.1 and 0.2 exhibited a noticeable improvement of the efficiency over the whole region, especially in the long wavelength region between 500 and 720 nm for MAPI−0.2MAI. The peak IPCE value of MAPI−0.2MAI exceeded 85% around 410 nm, and efficiency maintains above 60% in the range of 340−710 nm. Owing to the enhanced IPCE, the J_{sc} of MAPI−0.2MAI cells exhibited a pronounced improvement in photovoltaic performance. The J_{sc} vlaues for MAPI−0MAI, MAPI−0.1MAI, and MAPI−0.2MAI, integrated from their IPCE spectra and the AM 1.5G solar photon flux,[28] were 14.72, 15.37, and 17.08 mA cm^{-2}, respectively. The slightly lower J_{sc} obtained from IPCE spectra, compared to the values measured from the *J*−*V* curve, can probably be attributed to the surface traps of the TiO_2 layer.[26,29]

CONCLUSION

In summary, a new sequential deposition of $CH_3NH_3PbI_3$ absorber on mesoporous TiO_2 films was developed. Depending on the amount of MAI added in PbI_2 precursor solution, the crystallization of PbI_2 was enhanced with a low amount (*x* = 0.1

DOI: 10.1021/acsami.5b02705
ACS Appl. Mater. Interfaces 2015, 7, 12937−12942

and 0.2) and $CH_3NH_3PbI_3$ phase was formed with a high amount (x = 0.3 and 0.4) in as-prepared PbI_2−xMAI film. The PbI_2 phase was expected to be removed completely with a certain amount of addition of MAI, but PbI_2 was still detected even in MAPI−0.4MAI. With a low amount addition of MAI, the light absorption of $CH_3NH_3PbI_3$ increased without an obvious change of the surface morphology like grain size and flatness. In addition, the recombination rate of carriers can be reduced, implying the better quality of $CH_3NH_3PbI_3$. However, excessive addition of MAI not only increased roughness and lowered the surface coverage of capping layer but also embodied a higher recombination rate of carriers. Comparing with PbI_2−0MAI, the efficiency improved from 11.13% to 13.37% with optimal addition amount of PbI_2−0.2MAI. The improved device performance was attributed by enhanced J_{sc} and V_{oc}, which should be the result of higher light absorption and better quality of $CH_3NH_3PbI_3$ absorber. This method provided a new route for further improvement of device performance of $CH_3NH_3PbI_3$ solar cell fabricated by sequential deposition.

■ ASSOCIATED CONTENT

Supporting Information

Raman spectra, top-view FESEM images and AFM images of PbI_{2-x}MAI film, average device parameters of MAPI−xMAI solar cell, scan rate-dependent and scan direction-dependent J−V curves. The Supporting Information is available free of charge on the ACS Publications website at DOI: 10.1021/acsami.5b02705.

■ AUTHOR INFORMATION

Corresponding Authors

*E-mail: txu@niu.edu.

*E-mail: huangfq@mail.sic.ac.cn.

Notes

The authors declare no competing financial interest.

■ ACKNOWLEDGMENTS

The authors thank Prof. Yixin Zhao at Shanghai Jiao Tong University for kind suggestions and careful revision. This work was financially supported by National Science Foundation of China (Grants 91122034, 51125006, 61376056, and 61204072) and Science and Technology Commission of Shanghai (Grants 13JC1405700 and 14520722000). T.X. acknowledges support from the U.S. National Science Foundation (CBET-1150617).

■ REFERENCES

(1) Zhou, H.; Chen, Q.; Li, G.; Luo, S.; Song, T. B.; Duan, H. S.; Hong, Z.; You, J.; Liu, Y.; Yang, Y. Photovoltaics. Interface Engineering of Highly Efficient Perovskite Solar Cells. *Science* **2014**, *345*, 542−546.

(2) Jeon, N. J.; Noh, J. H.; Yang, W. S.; Kim, Y. C.; Ryu, S.; Seo, J.; Seok, S. I. Compositional Engineering of Perovskite Materials for High-Performance Solar Cells. *Nature* **2015**, *517*, 476−480.

(3) Chirilă, A.; Reinhard, P.; Pianezzi, F.; Bloesch, P.; Uhl, A. R.; Fella, C.; Kranz, L.; Keller, D.; Gretener, C.; Hagendorfer, H. Potassium-induced Surface Modification of $Cu(In,Ga)Se_2$ Thin Films for High-Efficiency Solar Cells. *Nat. Mater.* **2013**, *12*, 1107−1111.

(4) De Wolf, S.; Holovsky, J.; Moon, S.-J.; Löper, P.; Niesen, B.; Ledinsky, M.; Haug, F.-J.; Yum, J.-H.; Ballif, C. Organometallic Halide Perovskites: Sharp Optical Absorption Edge and Its Relation to Photovoltaic Performance. *J. Phys. Chem. Lett.* **2014**, *5*, 1035−1039.

(5) Xing, G.; Mathews, N.; Sun, S.; Lim, S. S.; Lam, Y. M.; Gratzel, M.; Mhaisalkar, S.; Sum, T. C. Long-Range Balanced Electron- and Hole-Transport Lengths in Organic-Inorganic $CH_3NH_3PbI_3$. *Science* **2013**, *342*, 344−347.

(6) Stoumpos, C. C.; Malliakas, C. D.; Kanatzidis, M. G. Semiconducting Tin and Lead Iodide Perovskites with Organic Cations: Phase Transitions, High Mobilities, and Near-Infrared Photoluminescent Properties. *Inorg. Chem.* **2013**, *52*, 9019−9038.

(7) Stranks, S. D.; Eperon, G. E.; Grancini, G.; Menelaou, C.; Alcocer, M. J.; Leijtens, T.; Herz, L. M.; Petrozza, A.; Snaith, H. J. Electron-Hole Diffusion Lengths Exceeding 1 Micrometer in an Organometal Trihalide Perovskite Absorber. *Science* **2013**, *342*, 341−344.

(8) Zhao, Y.; Nardes, A. M.; Zhu, K. Solid-State Mesostructured Perovskite $CH_3NH_3PbI_3$Solar Cells: Charge Transport, Recombination, and Diffusion Length. *J. Phys. Chem. Lett.* **2014**, *5*, 490−494.

(9) Kulkarni, S. A.; Baikie, T.; Boix, P. P.; Yantara, N.; Mathews, N.; Mhaisalkar, S. Band-Gap Tuning of Lead Halide Perovskites Using a Sequential Deposition Process. *J. Mater. Chem. A* **2014**, *2*, 9221−9225.

(10) Hao, F.; Stoumpos, C. C.; Chang, R. P.; Kanatzidis, M. G. Anomalous Band Gap Behavior in Mixed Sn and Pb Perovskites Enables Broadening of Absorption Spectrum in Solar Cells. *J. Am. Chem. Soc.* **2014**, *136*, 8094−8099.

(11) Eperon, G. E.; Stranks, S. D.; Menelaou, C.; Johnston, M. B.; Herz, L. M.; Snaith, H. J. Formamidinium Lead Trihalide: a Broadly Tunable Perovskite for Efficient Planar Heterojunction Solar Cells. *Energy Environ. Sci.* **2014**, *7*, 982−988.

(12) Lee, M. M.; Teuscher, J.; Miyasaka, T.; Murakami, T. N.; Snaith, H. J. Efficient Hybrid Solar Cells Based on Meso-Superstructured Organometal Halide Perovskites. *Science* **2012**, *338*, 643−647.

(13) Ball, J. M.; Lee, M. M.; Hey, A.; Snaith, H. J. Low-Temperature Processed Meso-Superstructured to Thin-Film Perovskite Solar Cells. *Energy Environ. Sci.* **2013**, *6*, 1739−1743.

(14) Zhao, Y.; Zhu, K. CH_3NH_3Cl-Assisted One-Step Solution Growth of $CH_3NH_3PbI_3$: Structure, Charge-Carrier Dynamics, and Photovoltaic Properties of Perovskite Solar Cells. *J. Phys. Chem. C* **2014**, *118*, 9412−9418.

(15) Colella, S.; Mosconi, E.; Fedeli, P.; Listorti, A.; Gazza, F.; Orlandi, F.; Ferro, P.; Besagni, T.; Rizzo, A.; Calestani, G.; Gigli, G.; De Angelis, F.; Mosca, R. $MAPbI_{3-x}Cl_x$ Mixed Halide Perovskite for Hybrid Solar Cells: The Role of Chloride as Dopant on the Transport and Structural Properties. *Chem. Mater.* **2013**, *25*, 4613−4618.

(16) Yu, H.; Wang, F.; Xie, F.; Li, W.; Chen, J.; Zhao, N. The Role of Chlorine in the Formation Process of "$CH_3NH_3PbI_{3-x}Cl_x$" Perovskite. *Adv. Funct. Mater.* **2014**, *24*, 7102−7108.

(17) Mosconi, E.; Ronca, E.; De Angelis, F. First-Principles Investigation of the TiO_2/Organohalide Perovskites Interface: The Role of Interfacial Chlorine. *J. Phys. Chem. Lett.* **2014**, *5*, 2619−2625.

(18) Shi, J.; Luo, Y.; Wei, H.; Luo, J.; Dong, J.; Lv, S.; Xiao, J.; Xu, Y.; Zhu, L.; Xu, X.; Wu, H.; Li, D.; Meng, Q. Modified Two-Step Deposition Method for High-Efficiency TiO_2/$CH_3NH_3PbI_3$ Heterojunction Solar Cells. *ACS Appl. Mater. Interfaces* **2014**, *6*, 9711−9718.

(19) Yongzhen, W.; Islam, A.; Yang, X.; Qin, C.; Liu, J.; Zhang, K.; Peng, W.; Han, L. Retarding the Crystallization of PbI_2 for Highly Reproducible Planar-Structured Perovskite Solar Cells via Sequential Deposition. *Energy Environ. Sci.* **2014**, *7*, 2934−2938.

(20) Jiang, Q.; Sheng, X.; Li, Y.; Feng, X.; Xu, T. Rutile TiO_2 Nanowire-Based Perovskite Solar Cells. *Chem. Commun.* **2014**, *50*, 14720−14723.

(21) Burschka, J.; Pellet, N.; Moon, S.-J.; Humphry-Baker, R.; Gao, P.; Nazeeruddin, M. K.; Grätzel, M. Sequential Deposition as a Route to High-Performance Perovskite-Sensitized Solar Cells. *Nature* **2013**, *499*, 316−319.

(22) Liu, D.; Yang, J.; Kelly, T. L. Compact Layer Free Perovskite Solar Cells with 13.5% Efficiency. *J. Am. Chem. Soc.* **2014**, *136*, 17116−17122.

(23) Sun, S.; Salim, T.; Mathews, N.; Duchamp, M.; Boothroyd, C.; Xing, G.; Sum, T. C.; Lam, Y. M. The Origin of High Efficiency in

DOI: 10.1021/acsami.5b02705
ACS Appl. Mater. Interfaces 2015, 7, 12937−12942

Low-Temperature Solution-Processable Bilayer Organometal Halide Hybrid Solar Cells. *Energy Environ. Sci.* **2014**, *7*, 399−407.
(24) Zhu, G.; Lin, T.; Lü, X.; Zhao, W.; Yang, C.; Wang, Z.; Yin, H.; Liu, Z.; Huang, F.; Lin, J. Black Brookite Titania with High Solar Absorption and Excellent Photocatalytic Performance. *J. Mater. Chem. A* **2013**, *1*, 9650−9653.
(25) King, R. R.; Bhusari, D.; Boca, A.; Larrabee, D.; Liu, X. Q.; Hong, W.; Fetzer, C. M.; Law, D. C.; Karam, N. H. Band Gap-Voltage Offset and Energy Production in Next-Generation Multijunction Solar Cells. *Prog. Photovoltaics Res. Appl.* **2011**, *19*, 797−812.
(26) Chen, Q.; Zhou, H.; Hong, Z.; Luo, S.; Duan, H. S.; Wang, H. H.; Liu, Y.; Li, G.; Yang, Y. Planar Heterojunction Perovskite Solar Cells via Vapor-Assisted Solution Process. *J. Am. Chem. Soc.* **2014**, *136*, 622−625.
(27) Hao, F.; Stoumpos, C. C.; Liu, Z.; Chang, R. P.; Kanatzidis, M. G. Controllable Perovskite Crystallization at a Gas-Solid Interface for Hole Conductor-Free Solar Cells with Steady Power Conversion Efficiency over 10%. *J. Am. Chem. Soc.* **2014**, *136*, 16411−16419.
(28) Joshi, U. A.; Maggard, P. A. $CuNb_3O_8$: A p-Type Semiconducting Metal Oxide Photoelectrode. *J. Phys. Chem. Lett.* **2012**, *3*, 1577−1581.
(29) Boschloo, G. K.; Goossens, A. Electron Trapping in Porphyrin-Sensitized Porous Nanocrystalline TiO_2 Electrodes. *J. Phys. Chem.* **1996**, *100*, 19489−19494.

DOI: 10.1021/acsami.5b02705
ACS Appl. Mater. Interfaces 2015, 7, 12937−12942